

Bachelor's Programme in Engineering Physics and Mathematics

The effect of carbon disulfide as a sulfur source in carbon nanotube synthesis and characteristics

Otto Salmela

© 2024

This work is licensed under a [Creative Commons](#)
“Attribution-NonCommercial-ShareAlike 4.0 International” license.



Author Otto Salmela

Title The effect of carbon disulfide as a sulfur source in carbon nanotube synthesis and characteristics

Degree programme Engineering Physics and Mathematics

Major Engineering Physics

Teacher in charge Prof. Esko I. Kauppinen

Advisor Dr. Ghulam Yasin

Date Number of pages 36+1 **Language** English

Abstract

Single-walled carbon nanotubes (SWCNTs) are a promising nanostructure with a variety of possible applications thanks to their unique properties such as mechanical, electrochemical and conductive properties. Despite decades of rigorous research since their discovery in 1991, many challenges remain today in synthesizing carbon nanotubes (CNTs) particularly selective growth of CNTs, scalability and reproducibility. Floating catalyst chemical vapor deposition (FCCVD) offers a promising synthesis method, which tackles multiple challenges through for example the continuous output of CNTs.

The inclusion of a growth promoter in the synthesis of CNTs has been studied extensively, and various elements have been used, of which sulfur has shown the most promise. The exact effect of sulfur in the synthesis remains unknown, and thus further studies to advance our understanding are needed. This paper explores particularly the effect of carbon disulfide (CS_2) as a sulfur source in the synthesis and characteristics of transparent conducting films (TFCs) of CNTs. The CNTs were found to minimize in diameter to about 1.3 nm with an optimum content of sulfur according to ultraviolet-visible-near infrared (UV-Vis-NIR) characterizations. Additionally, a lowest sheet resistance of $77 \Omega/\square$ at 90 % transmittance was attained for the synthesized TCFs. Diverse characterizations with Raman spectroscopy and also transmission electron microscopy (TEM) were additionally utilized, along with the ones mentioned, to further the understanding of CS_2 in the resulting CNTs.

Keywords Single-walled carbon nanotube, growth promoter, floating catalyst chemical vapor deposition, transparent conducting film

Tekijä Otto Salmela

Työn nimi Hiilidisulfidin vaikutus rikkilähteenä hiilinanotuubien synteesissä ja ominaisuuksissa

Koulutusohjelma Teknillinen fysiikka ja matematiikka

Pääaine Teknillinen fysiikka

Vastuuopettaja Prof. Esko I. Kauppinen

Työn ohjaaja Dr. Ghulam Yasin

Päivämäärä

Sivumäärä 36+1

Kieli englanti

Tiivistelmä

Yksiseinäiset hiilinanoputket ovat lupaavia nanorakenteita, joilla on monia mahdollisia sovelluksia niiden ainutlaatuisten ominaisuuksien, kuten mekaanisten, elektrokiemallisten ja johtavuusominaisuksien ansiosta. Vaikka hiilinanoputkia on tutkittu intensiivisesti niiden löydöstä vuonna 1991 lähtien, monia haasteita on edelleen, erityisesti hiilinanotuubien valikoivassa kasvussa, skaalaamisessa ja toistettavuudessa. Kaasufaasin katalyytin kemiallinen pintakasvatus tarjoaa lupaavan synteesimenetelmän, joka ratkaisee useita haasteita esimerkiksi hiilinanotuubien jatkuvalla tuotannolla.

Kasvunedistäjän käyttö synteesiprosessissa on laajalti tutkittu, ja erilaisia alkuaineita on käytetty, joista rikki on osoittautunut lupaavimmaksi. Rikin tarkka vaikutus synteesissä on kuitenkin edelleen tuntematon, ja lisätutkimuksia tarvitaan ymmärryksen syventämiseksi. Tässä tutkimuksessa tarkastellaan erityisesti hiilidisulfidin (CS_2) vaikutusta rikkilähteenä hiilinanotuubeista koostuvien läpinäkyvien johtavien kalvojen synteesissä ja ominaisuuksissa. Hiilinanotuubien halkaisijan havaittiin pienenevän noin 1,3 nanometriin, kun rikkipitoisuus oli optimaalinen ultravioletti-näkyvä-lähi-infrapuna -karakterisointien mukaan. Lisäksi syntetisoiduilla johtavilla kalvoilla saavutettiin alhaisin pintavastus, $77 \Omega/\square$, 90 % valonläpäisevyyddellä. Monipuolisia karakterisointeja, kuten Raman-spektroskopian ja myös läpäisyelektronimikroskopian, käytettiin, jotta ymmärrys CS_2 :n vaikutuksesta syntetisoituihin hiilinanotuubeihin syvenisi.

Avainsanat Yksiseinäinen hiilinanoputki, kasvunedistäjä, kaasufaasin katalyytin kemiallinen pintakasvatus, läpinäkyvä sähköjohdekalvo

Contents

Abstract	3
Abstract (in Finnish)	4
Contents	5
Abbreviations	6
1 Introduction	7
2 Theory	8
2.1 Carbon nanotubes	8
2.2 Synthesis process and methods	9
2.2.1 Arc-discharge and laser ablation	9
2.2.2 Chemical vapor deposition methods	10
2.3 Sulfur effect	11
2.4 Characterization methods	13
2.4.1 Sheet resistance	13
2.4.2 UV-Vis-NIR spectroscopy	13
2.4.3 Raman spectroscopy	14
2.4.4 Transmission electron microscopy	15
2.5 Doping	15
3 Research methods and equipment	17
3.1 The reactor	17
3.2 Compounds and solution preparation	18
3.3 Measurements and equipment	18
4 Results and discussion	20
4.1 Sulfur content	20
4.2 Feeding rate adjustment	24
4.3 Reactor temperature	25
4.4 Ferrocene content	27
4.5 Carrier gasses	30
5 Summary	32
References	33
A Results tables	37

Abbreviations

CNT	Carbon nanotube
SWCNT	Single-walled carbon nanotube
MWCNT	Multi-walled carbon nanotube
CVD	Chemical vapor deposition
CCVD	Catalytic chemical vapor deposition
FCCVD	Floating catalyst chemical vapor deposition
TCF	Transparent conducting film
UV-Vis-NIR	Ultraviolet-Visible-Near Infrared
TEM	Transmission electron microscopy
ITO	Indium tin oxide

1 Introduction

Carbon nanotubes (CNTs) and in particular single-walled carbon nanotubes (SWCNTs) have a wide variety of possible applications in different fields of technology owing to their unique and promising properties such as good conductivity, elasticity and electrochemical properties [1, 2]. These applications include for example transistors, batteries and importantly transparent conducting films (TCFs), which are used in, for example, touchscreen and solar cell applications [2, 3]. CNTs offer a possible improvement to industry standards, like indium tin oxide (ITO) in thin films, due to their cost-effectiveness, sustainability and unique properties. However, multiple major challenges in the synthesis of CNTs are still present after decades of rigorous research, such as the selective growth of CNTs with desired characteristics, scalability and reproducibility [4]. Tweaking starting parameters and synthesis conditions offer a way to tackle the aforementioned challenges.

There are a wide variety of synthesis methods used for CNTs which include for example arc-discharge, laser ablation, chemical vapor depositions (CVDs), in particular floating catalyst CVD (FCCVD), which offers advantages such as continuous output and scalability [3]. For the synthesis, carbon source and catalyst precursors are needed. A wide variety of carbon sources have been applied, but the most common ones are hydrocarbons such as ethanol, toluene, methane and ethylene, but additionally greenhouse gasses such as carbon monoxide and waste products are common precursors [4]. The catalyst particles, which act as a site for the CNT to start growing on, are usually transition metals such as iron, cobalt, nickel etc. Thus, especially organometallic compounds such as ferrocene are used for the synthesis [3].

In addition to carbon and catalyst precursors a growth promoter is commonly used, especially in FCCVD, which increases catalytic activity thus increasing the yield of CNTs [4]. Sulfur has been found to be a good growth promoter and has thus become a standard in the industry. Many theories for its effect in the synthesis process have been presented, such as lowering the melting point of catalyst particles, poisoning catalyst particle sites and lowering iron-carbon bond energies, but the exact role of sulfur in the process remains unclear [5]. Different compounds of sulfur intrinsically result in different outcomes for the synthesized CNTs, and the most commonly used compound remains thiophene.

The conducted work focuses on investigating and understanding the effect of carbon disulfide (CS_2) as a growth promoter on the synthesis and characteristics of the produced CNTs and their relevant differences compared with thiophene. To the best of our knowledge, no comprehensive study has been conducted on the FCCVD synthesis method using different amounts of CS_2 . Therefore, we will investigate the effect of varying sulfur ratios in the precursor feed, with particular focus on the yield of CNTs and physical characteristics, such as CNT diameter. This thesis will first delve into general theory pertaining to the synthesis of CNTs, after which the research methods and equipment will be presented. Next, the results will be presented and discussed and finally a summary of the thesis and work is given.

2 Theory

2.1 Carbon nanotubes

The discovery of the CNT structure is often credited to a 1991 study conducted by Sumio Iijima and his group, and is one of many interesting carbon nanostructures [6]. Other notable carbon nanostructures are for example graphene and fullerene. A fullerene can be thought of as a hollow ball-like structure comprised of carbon atoms, and graphene can be thought of as a two-dimensional sheet of carbon atoms. In graphene, carbon atoms form bonds with three nearest neighboring carbon atoms, forming hexagonal shapes in the lattice structure [1]. A CNT can be thought of as a graphene sheet which has been rolled-up to form a hollow cylinder, but it is important to note that CNTs do not grow this way during synthesis. CNTs can either be single-walled or multi-walled, where multiple CNTs are coaxially around each other. CNTs vary in length and diameter, but generally SWCNTs are 0.7-2.5nm in diameter, but a SWCNT of diameter as low as 0.3 nm was grown and found in a MWCNT structure [1].

As mentioned in the introduction, CNTs have a wide variety of different properties that make them applicable to multiple different fields of technology. Thanks to their structure, CNTs have great mechanical properties such as high tensile strength, elasticity and a Young's modulus up to 1-1.8 TPa which make them fare well under stress and bending. CNTs have great electrical properties such as high conductivity and current flow density which surpasses that of some metals such as copper. Additionally, they have great optical properties such as transparency while maintaining great electrical properties. CNTs also possess great thermal properties such as thermal conductivity, great chemical properties and a myriad of additional properties along with the ones mentioned here. These diverse and unique properties make CNTs applicable for optoelectronics such as touchscreens and displays, sensors such as biomedical- and chemical sensors, composites, transistors and a plethora of other applications. [2]

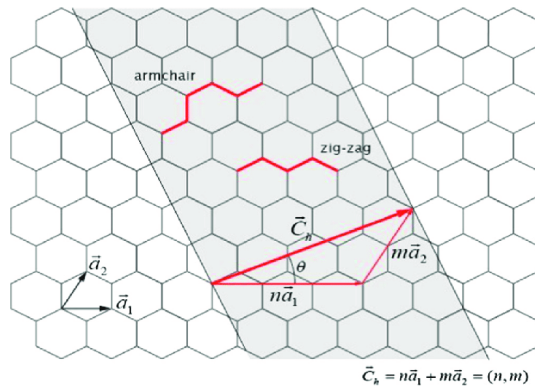


Figure 1: Diagram of the graphene lattice, chiral angle and chiral vector [7].

An important structural quantity of SWCNTs are the chiral indices (n, m). If we consider again a sheet of graphene and roll it up to form a cylinder, the angle at which

we roll it up, i.e. chiral angle, θ in figure 1, and the size of the tube affect the structure of the CNT. These are both uniquely determined by a chiral vector [7]:

$$\vec{C}_h = n \vec{a}_1 + m \vec{a}_2 \quad (1)$$

where the vectors \vec{a}_1 and \vec{a}_2 are the unit vectors of the graphene lattice, as seen in figure 1 [1]. If the chiral angle is 0° , then also m will be 0 and the resulting tube is called a zigzag tube, and if the chiral angle is 30° , i.e. when $n=m$, the resulting tube is called an armchair tube, and in all other cases the tube is called chiral [1]. The chiral indices (n,m) uniquely determine the structure around the circumference of the tube [7] and thus determine certain properties of the CNT such as electronic properties [1]. An important electronic property of a CNT is whether it exhibits metallic or semiconducting properties. If the difference $n - m$ is a multiple of three, then the CNT will be metallic, and otherwise it is a semiconductor, meaning that a third of CNTs are metallic [1]. Chirality control is thus a critical problem to tackle to optimize the CNTs for different applications. High semiconducting or metallic ratios of CNTs have been reported by tweaking synthesis parameters or applying posttreatment methods, but these are often reported with unreliable characterization methods, meaning metallic ratio control remains a challenge in CNT synthesis [3].

2.2 Synthesis process and methods

Throughout the years since their discovery, various methods have been developed and used to synthesize CNTs. Earlier methods include for example arc-discharge, which Sumio Iijima's group used in the original 1991 study, and laser ablation, but today CVD methods have become prevalent due to their superior control over the resulting nanotubes' characteristics [8]. This section will focus on covering these methods with a particular focus on floating catalyst CVD, which will be used in this study, and its advantages. It is important to note that these are not the only methods for CNT synthesis, and a multitude of other methods have been employed throughout the years since their discovery.

2.2.1 Arc-discharge and laser ablation

The arc-discharge method is one of the earliest synthesis methods for CNTs, along with fullerenes [8, 9]. The experimental setup consists of two graphite rods which are used as electrodes. Between these, an electrical current is maintained which is usually a direct current, but CNT formation with pulsed techniques are also possible [8]. The electrodes are brought together for a moment and an electric arc forms between them, resulting in carbon getting separated from the anode due to a very high temperature and a plasma forming between the electrodes [9]. Carbon deposits on the cathode and on other parts of the reactor, such as the walls, which can consist of amorphous carbon, SWCNTs, MWCNTs, fullerenes and even graphene [8, 9]. The arc-discharge synthesis method is particular because it doesn't require a catalyst precursor for CNT formation and in this case, MWCNTs are most commonly produced, but a catalyst can

be used in the form of a composite anode consisting of graphite and a transition metal, which results most commonly in the formation of SWCNTs [8]. Arc-discharge can be performed in a gas or liquid atmosphere with multiple different options for the nature of the atmosphere which intrinsically affects the results, and it produces a high yield of nanotubes but has a significant disadvantage in terms of their purity compared with other methods.

The laser ablation method most often consists of an experimental setup where a catalyst-carbon composite target inside a high-temperature furnace is hit by a laser beam. The laser vaporizes the target composite material, and the resulting soot is carried by carrier gasses to a cooled collection zone. The resulting CNTs are most often single-walled and have higher purity compared with the arc-discharge method, but a major disadvantage with this method is the smaller yield of CNTs. Again, synthesis parameters such as laser parameters, target composition, carrier gas parameters and furnace temperature affect diversely the synthesized CNTs and this method has been even successful at room temperature, without the need of a furnace. [9]

2.2.2 Chemical vapor deposition methods

CNT synthesis methods have faced numerous different challenges, such as low yields and poor control over the quality and structure of the nanotubes. There are multiple different types of CVDs, but catalytic chemical vapor deposition (CCVD) methods offer good control over the resulting CNTs and a scalable synthesis method while resulting in good quality CNTs [8, 9]. In these methods the carbon source decomposes with the help of for example hot-filaments, plasma or most commonly high temperature in the reactor [9]. CCVD methods most commonly employ a catalyst material supported on a substrate which is placed inside a reactor after which a hydrocarbon gas along with an inert gas (nitrogen, helium, argon) is injected into the reactor and made to decompose with the aforementioned methods which usually involves a furnace in the range of 600-1200 °C [8, 10]. After adequate time, the reactor will be cooled down and CNTs will be collected from the reactor walls and the substrate surface [10].

A common problem which CCVD methods, like the one described above, face is the scalability of the method and continuous output of CNTs. The floating catalyst CVD offers a solution to these and has various other advantages such as high yield, good quality, ease in constructing various macrostructures and good control over the structure of the CNTs [3, 11]. A typical experimental FCCVD setup consists of a feeding apparatus from which the precursors enter a high-temperature reactor (typically 1000 °C) along with carrier gasses such that the catalyst particles are floating around the gas atmosphere as an aerosol [3]. The CNTs are also thus in the gas atmosphere as an aerosol, and they will flow through the reactor to a collection unit, of which design depends on the macrostructure wanted.

The CNT growth mechanism depends largely on the used synthesis method, and in the FCCVD method it is believed to occur as follows. The precursors first start thermally decomposing inside the reactor and in this work the important thermal decompositions are decompositions of ethanol, ferrocene and carbon disulfide. The first of these to happen is the decomposition of ferrocene which occurs spontaneously

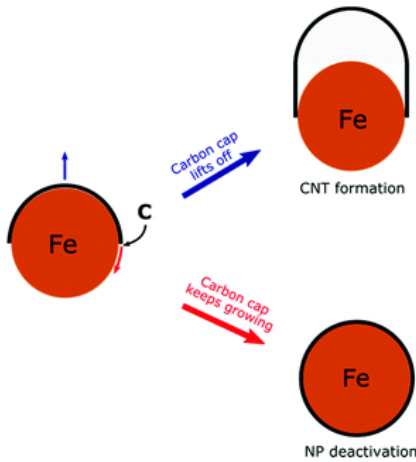


Figure 2: Carbon cap formation and nanoparticle deactivation on the catalyst particle surface [12].

at 500 °C following the reaction $Fe(C_5H_5)_2 \rightarrow Fe + H_2 + CH_4 + C_5H_6+$ reactive hydrocarbons [13]. The catalyst particles i.e. iron particles nucleate and grow through collisions which form a foundation for the CNTs to start growing on [3]. The thermal decomposition of ethanol starts at approximately 525 °C [14] having multiple possible ways of decomposing which result in products such as ethylene, hydrogen, hydroxide, water etc. [15]. The most important final product of this decomposition process is the resulting carbon radicals, which start diffusing on the catalyst particle surfaces and forming a carbon cap [12, 11]. An illustration of this can be seen in figure 2. The carbon can either continue to precipitate on the catalyst surface resulting in the deactivation of the particle or the carbon cap can lift off and a CNT will start growing from the base. The decomposition of CS_2 starts at 650 °C, resulting in both carbon and sulfur radicals [16]. The effect of sulfur in the synthesis process will be covered in more detail in the following section, but it is believed to aid in the carbon cap lift off process [12, 5].

2.3 Sulfur effect

As mentioned earlier, the exact role of sulfur in the synthesis process and CNT growth mechanisms remains unclear since *in situ* imaging and investigation of the process is extremely difficult and thus the only ways to determine the role of sulfur are through computer simulations, judging the synthesis product and applying known sulfur effects and characteristics to form theories. Nevertheless, sulfur has been widely confirmed to act as a growth promoter, heavily increasing the yield of CNTs, and also to diversely affect the CNT properties based on the compound used [5]. The most common of these remains thiophene but compounds such as hydrogen sulfide, bithiophene and carbon disulfide have also been employed, the last of which is used in this work and will be at the forefront of focus.

The mechanistic behavior of sulfur with the catalyst particle during the synthesis process is divided into two main theories. The first of these is its "poisoning" effect on

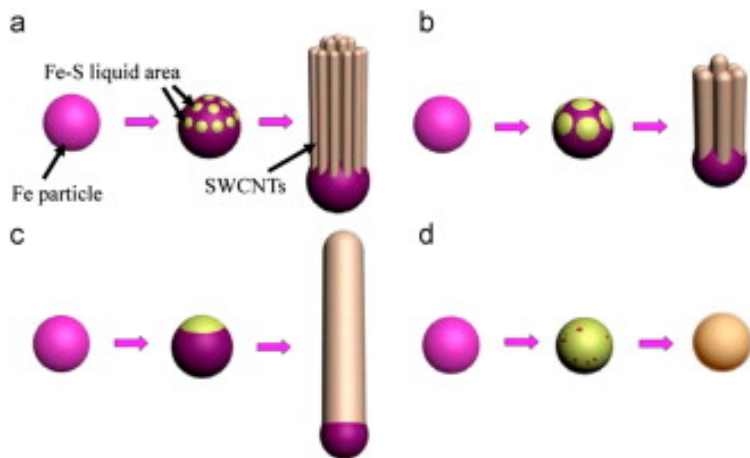


Figure 3: Possible proposed effects of sulfur on the catalyst particle surface [17].

the catalyst particle, where sulfur forms Fe-S bonds on the particle surface and the CNT starts nucleating on sites not occupied by the sulfur, for example in figure 2 if the underside of the particle was coated with sulfur [1, 5]. This effectively restrains the diffusion of carbon on the nanoparticle surface geometrically and electronically (sulfur donating electrons to the metal), ensuring that nanoparticle deactivation does not occur [5]. The presence of the sulfur is known to also have an effect on the binding energies between the nanoparticle and other reactants, which could also mean a significant reduction in the binding energy between the catalyst and the carbon cap, aiding in the lift-off and growth of the CNT, which is supported by a DFT simulation study and some *in situ* observations of the nanoparticle [4, 5, 12].

The other theory for the effect of sulfur is heavily supported by this reduction in the binding energy between the CNT and the catalyst particle. This effect proposes that the nanotube starts nucleating on sites occupied by sulfur, which can be seen in figure 3a-c [5, 12]. The reduced binding energy would attract the carbon atoms and result in easy and fast CNT nucleation on sites rich with sulfur, and the amount of sulfur on these sites would determine the diameter of the CNTs. The presence of sulfur on the nanoparticle surface has been shown with an electron energy loss spectroscopy study where sulfur was observed mostly on the CNT side which would support the latter theory but nevertheless sulfur is known to attach to the catalyst surface even if the exact growth mechanism is not entirely clear, but it is important to note that it does not incorporate itself into the CNT lattice [5]. An excess amount of sulfur could thus coat the entire catalyst particle, resulting in catalyst deactivation, as can be seen in figure 3d.

Through coating the catalyst particle, sulfur has a variety of additional effects on its properties along with the lowering of binding energy for the carbon. The absorption energy has been shown to decrease for compounds such as CO and H_2 decreasing the covering due to unwanted compounds [5]. Other well known effects are the lowering of the melting point of the metal particle which in turn enhances carbon diffusion on the particle surface, exponential sulfur increase on the catalyst surface and surface tension of the particle decreasing [5].

An addition of sulfur in the synthesis has been widely shown to increase yield, diameter, walls and length of the CNTs which usually leads to a bell-shaped curve where these achieve extrema at optimum sulfur contents [1, 5, 4]. The increase in yield and length can be attributed to sulfur aiding the carbon cap lift-off and also increasing the number of active catalyst particle, and the diameter increase could be due to a variety of changes between the carbon and metal, such as delaying of the nucleation, leading to larger catalyst particles and CNTs [5]. It is important to note however that the diameter has been observed to decrease in a few cases which can be attributed to coating by sulfur radicals on the surface restricting the nucleation of the catalyst particles and also some compounds having a lower decomposition temperature, making them available to coat the particles earlier [5, 18, 19]. Sulfur has also been shown to result in chiral selectivity, with chiralities such as (7,6) shown to be more likely in the case of CS_2 and (9,8) being dominant in a variety of cases [5].

2.4 Characterization methods

2.4.1 Sheet resistance

The resistance of a three-dimensional material can be calculated from the equation:

$$R = \rho \frac{L}{A} = \frac{\rho}{t} \frac{L}{W}, \quad (2)$$

where ρ is the resistivity of the material, L is the length, W the width and t the thickness of the conductor. The quantity $\frac{\rho}{t}$ is also known as the sheet resistance R_s of a conducting film of specific thickness which will be the same when over any square, i.e. when $L = W$. The sheet resistance is thus often given in the unit Ω/\square (ohms per square).

A number of different methods for determining the sheet resistance of a conductive thin film have been fabricated, but the most common and simplest remains the four-point probe method [20]. A four-point probe apparatus consist of four equally spaced probes in a line and a direct current will be applied through the outermost probes, which results in a voltage difference between the inner probes and can then be measured. The sheet resistance can then be calculated from the equation [20]:

$$R_s = \frac{\pi}{\ln 2} \frac{\Delta V}{I}, \quad (3)$$

where ΔV is the voltage difference between the inner probes and I is the applied current.

2.4.2 UV-Vis-NIR spectroscopy

Ultraviolet-Visible-Near Infrared (UV-Vis-NIR) spectroscopy is a technique of optical absorption used to determine various optical properties of both liquids and solids. In this spectroscopy method, light in the UV to near infrared range is passed through a material which will absorb a portion of the light, giving us an absorption spectra in the desired range of light. In the case of CNTs, a π plasmon peak at low wavelengths and

peaks called the van Hove singularities will be present in the spectra, which correspond to different excitations of electrons between the valence and conduction bands of the CNT as they absorb energy from the incoming light [1]. The most important of these transitions, which will be visible in the range of the spectra and used to calculate various quantities, are S_{11} , S_{22} and M_{11} . Here S or M means a transition in a semiconducting or metallic CNT respectively and the numbers indicate from which band the electron has jumped from and to which it has transitioned to, for example S_{11} means from the first valence band to the first conduction band.

An approximate for the mean diameter of the CNTs can be calculated from the position of any of the peaks, for example using the energy E_{22}^S corresponding to the wavelength of the S_{22} peak, we get the equation [21]:

$$d = \frac{4a_0\gamma_0}{E_{22}^S}, \quad (4)$$

where a_0 is the distance of the C-C bond and γ_0 is the interaction energy between neighboring C atoms, which are approximately 0.142 nm and 3.0 eV respectively [22, 23].

The metallic to semiconducting nanotube ratio can also be approximated from the UV-Vis-NIR spectra with the help of the van Hove peaks and the mean diameter. Using the S_{22} and M_{11} peaks, we first obtain the integrated intensities of these peaks in reference to the baseline of the spectra, which can then be used to calculate the metallic ratio of nanotubes with the equation [24]:

$$R_{Metal} = \frac{1}{1 + d \frac{I_{S22}}{I_{M11}}}, \quad (5)$$

where I_{S22} and I_{M11} are the integrated intensities of the peaks. This method for determining the metallic ratio of CNTs in a macroscale material is however a rough approximation and for better estimations other methods such as transmission electron microscopy (TEM) should be used.

Finally, the transmittance of the material can be calculated with the help of the Beer-Lambert law [25]:

$$A = \log_{10} \left(\frac{I_0}{I} \right), \quad (6)$$

where A is the absorbance, I_0 is the intensity of the light beam and I is the intensity of the beam after transmitting through the material meaning this ratio is the inverse of the transmittance T of the material and thus the transmittance can be calculated from:

$$T = 10^{-A}. \quad (7)$$

2.4.3 Raman spectroscopy

Raman spectroscopy is based on photons inelastically scattering when interacting with a material [26]. In inelastic scattering, the wavelength of the incident laser has been shifted through interaction with the material, in this case due to the light responding

to the vibrational modes in the material. This is called the Raman shift, often given in the unit cm^{-1} representing the shift in wavelength and thus the shift in energy. For a SWCNT sample, multiple different peaks will be present in these spectra, which tell us about the properties of the CNTs. These include the radial breathing mode (RBM), D, G, 2D or G' bands. The RBM band is unique for CNTs and is seen at low Raman shifts around $100\text{--}200\text{ }cm^{-1}$ and is associated with the radial vibrational mode of the cylindrical shape [1, 26]. The G band, which is often seen in carbon materials, is located around $1580\text{ }cm^{-1}$ and is divided into two sub-bands, G^+ and G^- , where the former comes from the vibrational mode along the axis of the tube and the latter from the mode along the circumference of the tube [1]. The D band is seen at around $1350\text{ }cm^{-1}$ and is often associated with defects in the sample such as catalyst particles, amorphous carbon etc. meaning its intensity can be used to determine the quality of the sample [1]. The 2D (or G') band is seen at around $2700\text{ }cm^{-1}$ and its exact location depends on the wavelength of the laser used and while its name would suggest it also implies defects in the sample, it has no relation to defects [26]. The frequency of the RBM band is proportional to the diameter with the formula:

$$\omega_{RBM}\left(cm^{-1}\right) = \frac{A}{d} + B, \quad (8)$$

where A and B are experimentally determined constants for SWCNT films, which are 217.8 and 15.7 respectively [1]. This can be used to approximate the diameter distribution with the specific intensities in the Raman spectra, but it is important to note that specific lasers excite only a portion of CNTs in the sample and thus a single laser will not give us a comprehensive idea on the diameters of CNTs in the sample.

2.4.4 Transmission electron microscopy

Transmission electron microscopy is a material imaging method where an electron beam is passed through a thin sample and through interactions like scattering between the electron and the material, an image can be formed. TEM offers a far better resolution compared with light imaging, thus giving us precise images of the structure of the sample. In the case of CNTs, accurate bundle size and CNT diameter distributions can be produced, and also catalyst particles can easily be investigated. Along with these, electron diffraction can be used to determine the chirality of singular nanotubes and is one of the most reliable ways of mapping chiralities in a specific sample [1, 27].

2.5 Doping

Doping generally means when a different particle replaces a particle from a homogeneous lattice structure, altering its properties through donating an electron or creating an electron hole. This alters the density of states of the whole material, where if the new states created by the doping are above the Fermi-energy of the undoped CNT i.e. if the replacement has more valence electrons than carbon, it will shift the Fermi-energy toward higher energies [28]. This can result in the lower energy conduction bands getting filled with electrons due to the Pauli exclusion principle, thus improving the

conductivity of the CNT [29]. The conduction bands getting filled also result in the aforementioned van Hove transitions becoming impossible since the bands are occupied, and thus the peaks will start to disappear from the UV-Vis-NIR spectra starting with S_{11} . The doping effect of ambient air is also well known to improve the conductivity of CNTs where oxygen, which has six valence electrons compared to carbons four, is normally acting as the dopant [30].

3 Research methods and equipment

3.1 The reactor

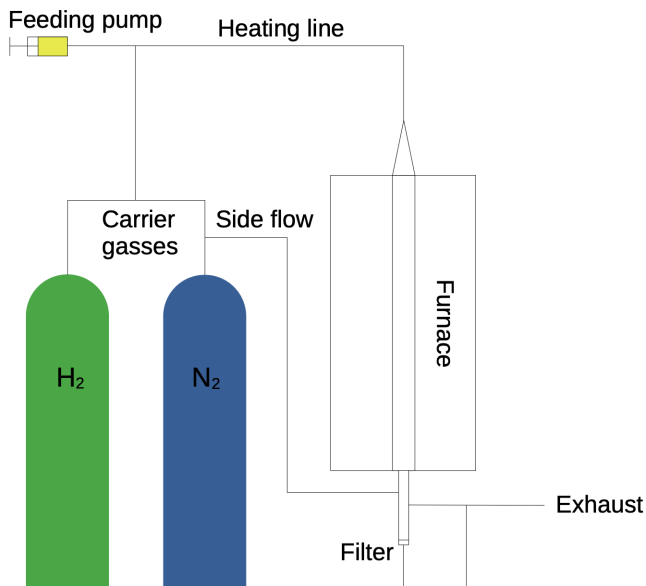


Figure 4: Schematic of the FCCVD reactor.

For the synthesis of the CNTs, the FCCVD method is used in this thesis and a schematic of the FCCVD reactor which was used can be seen in figure 4. The reactor setup consists of feeding, carrier gas, furnace, and collection components. A syringe coupled to a pump (NE-1000 Syringe pump, New Era Pump Systems Inc.) is used as the method for a liquid feed, which can be precisely controlled and is kept at 3 $\mu\text{l}/\text{min}$. The solution is evaporated in a heating line kept at 150 °C and carried to the reactor by carrier gasses of nitrogen (N₂) and hydrogen (H₂) along with a side flow of nitrogen. The side flow is kept at 2 l/min throughout this study and the carrier gasses are first kept both at 400 SCCM so 50/50 of N₂ and H₂ after which they will be adjusted to see their effect.

The solution along with the gasses arrives at the reactor as an aerosol, where it enters a quartz tube, which is heated by a furnace at the center. The reactor is first kept at 1050 °C, after which we will adjust this in the range of 950-1100 °C to see its effect. With the heating zone on the quartz tube being in the middle of the tube, the temperature inside the reactor drops towards the ends of the quartz tube. Inside the reactor, ethanol, ferrocene and CS₂ start thermally decomposing and the synthesis process for CNTs begins. These CNTs are then collected on a membrane filter (0.45 μm pore size, MF-Millipore™) or exhausted through a vacuum trap (Visi-Trap® Vacuum Trap, Mass-Vac Inc.) to filter out the CNTs if the bypass valve is switched and CNTs are not being collected. The collection times will be varied, and multiple samples will be collected for each solution to end up with adequate amount of data and CNT films with different transmittances. From the membrane filter the CNT film

can be transferred to a glass substrate by pressing and removing the filter which can then be characterized. A side flow is necessary to ensure adequate flow due to the relatively low amount of carrier gas flow so that the CNT film collected on the filter will be consistent, but it will not affect the synthesis conditions since it does not enter the reactor.

3.2 Compounds and solution preparation

The liquid solution which is fed into the reactor consists of three compounds: carbon, catalyst and sulfur precursors. In this thesis ethanol (EtOH, $\geq 99.5\%$, Anora Industrial) is used as the carbon source, ferrocene ($\text{Fe}(\text{C}_5\text{H}_5)_2$, 99%, Alfa Aesar) as the catalyst precursor (iron being the catalyst particle) and carbon disulfide (CS_2 , $\geq 99\%$, Sigma-Aldrich) as the sulfur precursor. The weight percentage (wt%) of ferrocene to the rest of the solution and the molar ratio of S/Fe are the important quantities to consider when producing the liquid solution. In this thesis, we will first examine how changing the S/Fe ratio affects the resulting CNTs by changing the ratio in the range of 0.1-2.0. After this, we choose a candidate S/Fe molar ratio and change the wt% of ferrocene in the range of 0.1-0.5.

To prepare the solution, first the necessary amounts of ethanol, ferrocene, and CS_2 for the appropriate weight percentage and S/Fe ratio will be calculated. For example, for 0.3 wt% and 0.3 S/Fe ratio, 4.7 g of ethanol, 14.2 mg of ferrocene and 0.7 μl of CS_2 is required. These can all be scaled accordingly to end up with a larger solution while retaining the ratios, which was done to lower the error associated with measuring small amounts of CS_2 . After the calculations, the ferrocene and ethanol will be measured on a precision scale (AS 101.R2, Radwag) after which the CS_2 is measured on a manual single channel pipette (FinnpipetteTM F2, Thermo Fisher Scientific). The resulting solution is then sonicated (Ultrasonic cleaner, VWR[®]) to ensure the ferrocene has dissolved fully into the solution.

3.3 Measurements and equipment

After the CNT film has been transferred to a glass substrate for characterizations, the sheet resistance will be immediately measured with a four point probe (RM3000/RM3000+, Jandel) by measuring at multiple points in the film to ensure accurate readings. The sheet resistance will be measured again for all samples after a minimum of a week to ensure adequate ambient doping due to air has occurred. Air is also known to purify the CNTs films of impurities like hydrocarbons, which improves the samples further. Some samples will be additionally doped by drop-casting three droplets onto the film surface of 16 mM gold chloride (AuCl_3) dissolved in isopropyl alcohol (IPA). These will be left to dope for a day in a fume hood, after which they will be washed with IPA and left to dry off for an additional day. After this, the sheet resistance will be measured with the same methodology as before. The sheet resistance will be compared with the industry standard ITO, which can be as low as approximately $10 \Omega/\square$ [31].

The CNT film will also be characterized by UV-Vis-NIR spectroscopy (Cary 5000 UV-Vis-NIR Spectrophotometer, Agilent Technologies) from which absorbance spectra will be produced. From the UV-Vis-NIR spectra multiple quantities such as, metallicity, average diameter and transmittance at 550 nm are calculated and graphs will be produced. The transmittance is measured at 550 nm since it lies in the middle of the visible range of light and thus represents the transmittance for all visible light well. The resistance at 90 percent transmittance can be calculated with the help of the transmittance and sheet resistance from [27]:

$$R_{90} = R_s \log_{0.9} T, \quad (9)$$

which will be shown as graphs. Along with these quantities, the productivity of the synthesis process can be measured as the yield of the CNTs, for which graphs will also be presented. This is calculated with the help of the transmittance of the collected thin film from the equation [27]:

$$Yield \left[\frac{cm^2}{L} \right] = \frac{S}{Q \cdot t} \log_{0.9} T, \quad (10)$$

where S is the filter collection area, t the collection time and Q the reactor flow rate. For all these quantities, mean values of all samples will be used for plotting and the standard deviation for the samples is used to produce error bars. The transmittances at 550 nm along with the sheet resistances can be used to create transmittance vs. sheet resistance graphs, from which we can see which films fare best in terms of conductivity. An empirical equation can be fitted on the data [32]:

$$T = e^{-\frac{1}{K \cdot R_s}}, \quad (11)$$

where K is a coefficient of proportionality which determines the quality of the film in terms of conductivity.

The Raman spectra is measured with a spectrometer (Horiba Jobin-Yvon Labram HR 800) with a 514 nm laser, and a spectrum for one sample from each condition will be produced. These will be shown and compared in graphs, and also equation 8 will be used to show a diameter axis with the RBM peak to get an approximate for the diameter distribution. The size of the D band will also be evaluated to determine the quality of the sample.

For the TEM imaging, the CNTs were collected on a copper substrate for 10 seconds and three drops of toluene followed by three drops of acetonitrile were drop-casted onto the thin film to clean and densify the samples. These were then left overnight in a vacuum to fully evaporate any moisture and ensure cleanliness. TEM micrographs were collected with an electron microscope (JEM-2200FS, JEOL) and will be presented at various magnification levels.

All experimental data obtained from the UV-Vis-NIR spectra, four point probe measurements and Raman spectra including diameters, metallic ratios, doped R_{90} values and yields are gathered in individual tables in the appendix A. Thus, if specific values are needed, one can refer to the appendix.

4 Results and discussion

4.1 Sulfur content

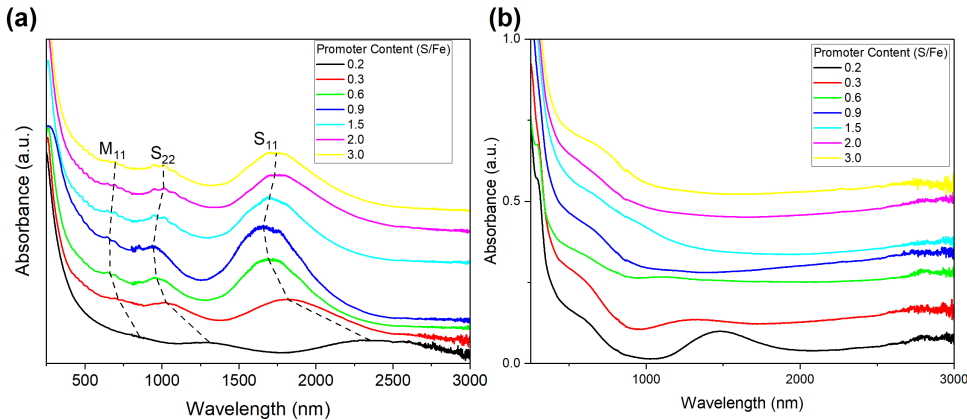


Figure 5: UV-Vis-NIR spectra of (a) pristine (b) $AuCl_3$ doped CNT films synthesized with different sulfur contents.

First, the sulfur to iron molar ratio was varied in the range of 0.2-3.0 to determine an optimum sulfur content. In addition to this, sulfur contents of 0 and 0.1 were tested, but the former resulted in no CNTs and the latter resulted in a very low yield and larger tubes of poor quality which blocked the reactor continuously, so no systematic data for these are presented. The UV-Vis-NIR spectra for the pristine sulfur contents investigated can be seen in figure 5a, where we can see the aforementioned van Hove peaks labeled S_{11} , S_{22} and M_{11} and also the π plasmon peak on the left. The spectra are vertically translated so that they do not overlap to aid readability, meaning the heights of the specific spectra are not relevant. All the UV-spectra in this work will be presented in this manner. The spectra for the $AuCl_3$ doped samples can be seen in 5b where most of the S_{11} , S_{22} and even M_{11} peaks have either completely disappeared or significantly reduced in intensity indicating significant doping has happened, which is to be expected, as was discussed in section 2.5. The doping effect can be observed to be smaller for smaller S/Fe ratios, as 0.2 and 0.3 exhibit smaller reductions in for example the S_{22} intensities.

Especially with higher sulfur ratios, we notice that particularly the S_{22} and M_{11} peaks seem to consist of multiple individual peaks, which could be an indication of CNTs of specific chiralities which sulfur is known to have an effect on as mentioned before. Already based on the spectra we can see that an optimum is reached at 0.9 S/Fe where the peaks correspond to the highest energies. The calculated averages of yield, diameter, R_{90} and metallic ratio can be seen in figure 6 a-d where we see yield and metallic ratio following the well-known bell-shaped curve where an optimum is reached at 0.9 S/Fe and at high sulfur contents the values start to drop and ultimately approach a saturation level. This behavior of the yield is exactly as expected from the literature. The average metallic ratios are all between 10 and 20 percent, meaning the

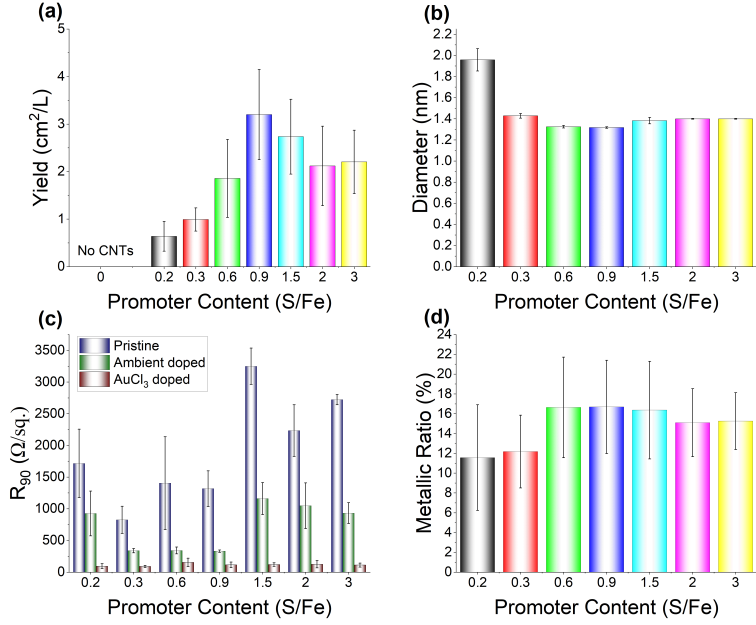


Figure 6: Bar graphs of (a) yield (b) mean tube diameter (c) sheet resistance at 90% transmittance (d) metallic ratio vs. sulfur content.

synthesis seems to favor semiconducting tubes considerably, but as mentioned before, these are rough estimates.

The behavior of the mean diameter is unexpected, where an optimum sulfur content minimizes the average diameter of the tubes. As mentioned earlier, sulfur is known to mainly increase the size of the CNTs, but the diameter decrease could be due to the aforementioned effect of catalyst particle nucleation restriction of sulfur. The average diameter increases slightly after 0.9 S/Fe, which could be explained due to catalyst deactivation through sulfur coating the catalyst particle which would naturally occur first for smaller catalyst particles, increasing the diameter distribution. This could also at least partly explain why the yield drops after the optimum is reached. An important question is why does this not occur with thiophene, where an optimum amount of sulfur maximizes the diameter. An explanation could lie in the difference in decomposition of thiophene and CS_2 , where the former results in hydrogen radicals in addition to carbon and sulfur radicals. These hydrogen radicals could play a part in reducing the blocking effect of the sulfur [19]. Additionally, CS_2 decomposes approximately 150 °C lower than thiophene, which means that the sulfur from CS_2 is available earlier to have a restricting effect on the catalyst particles, resulting in smaller particles and smaller CNTs.

The R_{90} values behave more erratically when compared with the rest of the quantities, where we see an optimum at 0.3 before doping and at 0.9 after ambient doping. The ambient doped values were measured in this case over a month after the synthesis of the films, so significant drop-offs are seen and expected. After doping with $AuCl_3$, the R_{90} seems to be the best with lower sulfur contents, 0.2 and 0.3 where

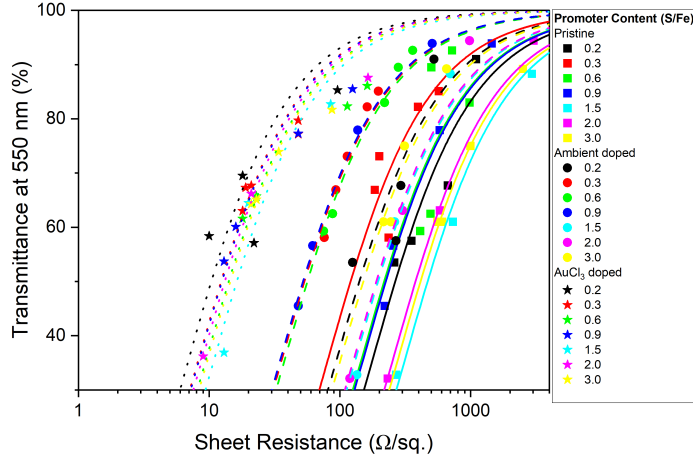


Figure 7: Transmittance vs. sheet resistance curves for pristine and doped values of different sulfur contents.

the R_{90} values were approximately 94 and 90 Ω/\square respectively. The same can be concluded from the resistance vs. transmittance graphs with undoped, ambient doped and $AuCl_3$ doped values in figure 7 a-b, where curves have been fitted to the data. An optimum at 0.3 before doping could occur because of the band gap increasing as diameter decreases, and thus larger nanotubes have higher conductivity [1]. The poor conductivity of CNTs synthesized with 0.2 or higher than 0.9 can be explained by poor quality of tubes in terms of conductivity, meaning significant amounts of amorphous carbon and possibly larger bundle size of CNTs [5]. At 0.9, this quality could be the best, resulting in the best values after ambient doping. After $AuCl_3$ doping, the samples are likely purified to some degree, and thus the samples with larger CNTs fare the best. We can also see from figure 7 that with higher transmittances, the doping results in poorer R_{90} values, which could be due to a significant difference in transmittance after doping, and this affects most the samples with higher transmittances.

The Raman spectra for each of the conditions can be seen in figure 8a-c. The diameters calculated from the RBM peak spectra coincide well with ones gotten from the UV-Vis-NIR spectra, where we can see that 0.2 is significantly larger than the others where the largest intensities are seen at approximately 1.3 nm and 0.9 having a lower intensity at approximately 1.6 nm compared with others meaning a smaller average diameter. Most of the spectra seem to favor these two approximate diameters, as their intensities are the largest. It is important to note, that even though the average diameter seems to decrease approaching 0.9 S/Fe, the diameter seems to be restricted to about 1.25 nm and does not get lower than this for any of the conditions. The D-band is negligible for all the samples and thus cannot be effectively used to compare the samples against each other in terms of quality, but all samples seem to be of good purity. The G^- -band seen on the left side of the peak is very prominent, meaning a high amount of CNTs are present. It is important to note that the Raman data is gathered from only one sample per condition and only with one laser, meaning that

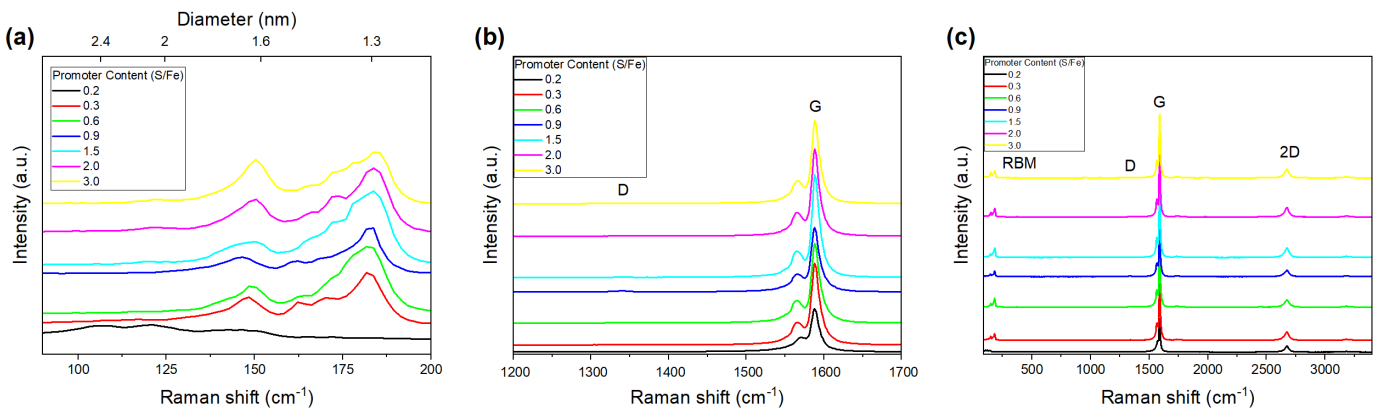


Figure 8: Raman spectra of CNT films synthesized with different sulfur contents. (a) shows the RBM band (b) shows the D and G bands and c) shows the whole spectra.

especially the diameter spectra is only an approximation. For a comprehensive Raman study, multiple lasers should be considered.

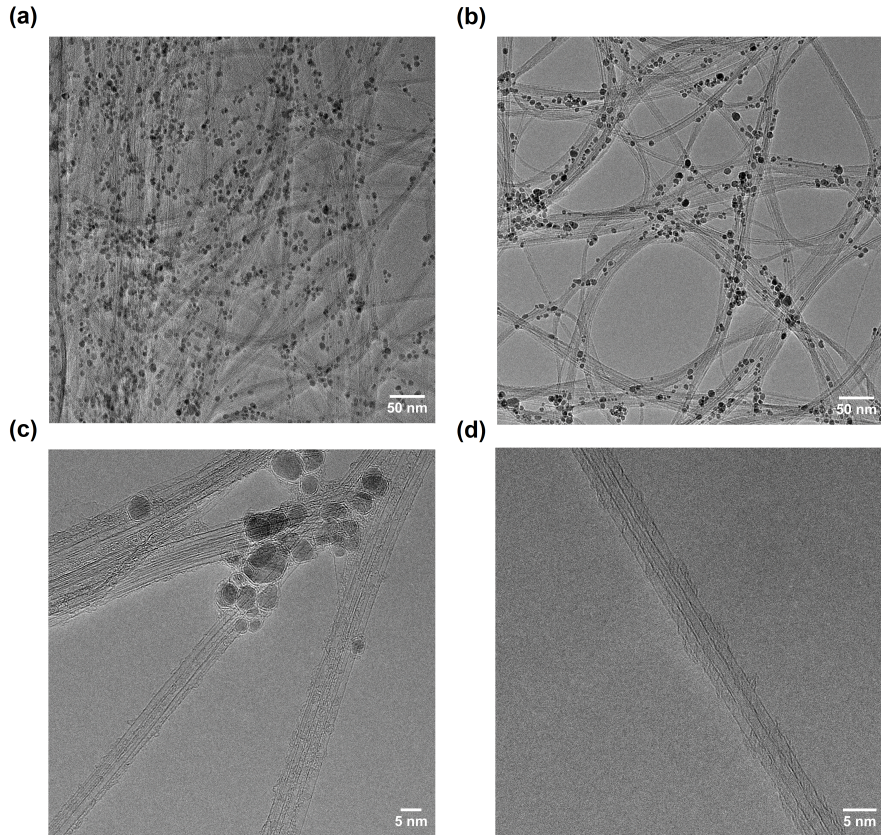


Figure 9: TEM micrographs of CNT networks synthesized with 0.9 sulfur content.

TEM images synthesized with 0.9 sulfur content can be seen in figure 9a-d with different magnification. In figure 9a-b we see a tremendous amount of catalyst particles

(darker circular masses) resulting in a diverse CNT network and numerous bundles. In figure 9c we see various bundles of CNTs and catalyst particles from up close. In figure 9d we see a singular CNT bundle consisting of three SWCNTs. The CNTs look to be mostly single walled, but some MWCNTs are definitely also present in the sample. For a comprehensive diameter and bundle size analysis from TEM, around one hundred singular CNTs and bundles should be considered resulting in distributions which approximate these quantities with good accuracy, but this is outside the scope of this thesis along with the chirality analysis through electron diffraction. 0.9 S/Fe was chosen for these images since it seemed to optimize the CNT synthesis when considering all the aforementioned quantities, and thus it will also be used for the experiments moving forward.

4.2 Feeding rate adjustment

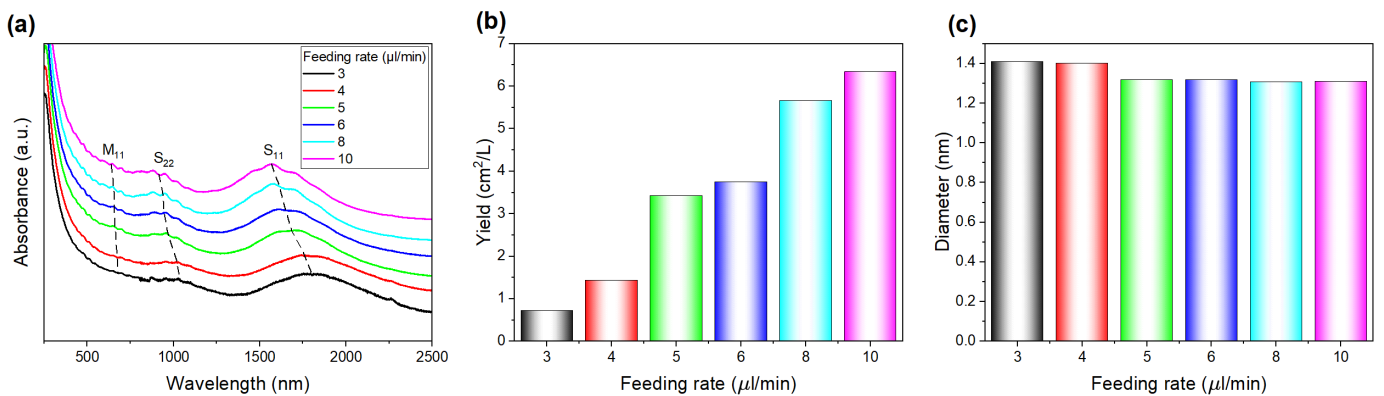


Figure 10: (a) UV-Vis-NIR spectra, (b) yield, and (c) average diameter at different feeding rates.

When moving on with the experiments, we quickly noticed a discrepancy between the new and old results with 0.9 S/Fe, namely the yield had gotten significantly worse. We believed that this could be due to an intrinsic difference in the actual feeding rate, even though the feeding pump used still reported 3 $\mu\text{l}/\text{min}$. We altered the feeding rate in the range of 3-10 $\mu\text{l}/\text{min}$ and noticed from the UV-Vis-NIR spectra presented in figure 10a that the feeding rate had an effect on the nanotube diameter. The results for the yield and diameter can be seen in figure 10b-c, and we can see that yield increases with increasing feeding rate, as expected, and diameter decreases. This decrease in diameter could be due to an increased amount of aerosol in the reactor and thus an increased amount of collisions between the particles inside, which could make the sulfur agglomerate on the catalyst particles' surface faster. It is important to note that only one stable sample was synthesized per feeding rate, hence no error bars, and thus this is not a comprehensive study on the effect of feeding rate. These results are only shown to justify our decision to adjust the feeding rate to 6 $\mu\text{l}/\text{min}$, since it seemed to reproduce our earlier results well. The following experiments are thus produced

with a $6 \mu\text{l}/\text{min}$ feeding rate, while the results in section 4.1 were synthesized using $3 \mu\text{l}/\text{min}$. Effectively, these seem to produce comparable results.

4.3 Reactor temperature

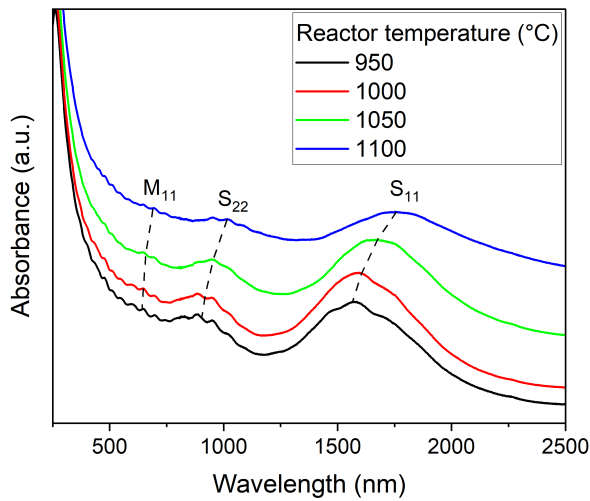


Figure 11: UV-Vis-NIR spectra of CNT films synthesized with different reactor temperatures.

The results for the UV-Vis-NIR spectra of samples synthesized with different reactor temperatures can be seen in figure 11 where we can see the peaks shifting right with increasing temperature and also significant rippling on the peaks. The peaks synthesized with $1100 \text{ } ^\circ\text{C}$ seem to also be broader in comparison to others, which could indicate a broader diameter distribution.

The calculated quantities from the UV-Vis-NIR spectra and sheet resistance measurements can be seen in figure 12, where we see the yield increasing up to $1050 \text{ } ^\circ\text{C}$, after which we see a drop likely due to increasing blockages in the reactor due to larger size CNTs. The diameter is observed to increase with reactor temperature, which also results in a lower sheet resistance as can also be seen in figure 13, likely due to a smaller band gap. Here the ambient doped values are after approximately a week of doping, so a smaller drop-off between these and the sulfur content results is to be expected. The reason why the diameter increases, could be due to the surface concentration of sulfur decreasing on the catalyst surface with increasing temperature [5]. This means that the restricting effect of sulfur on the catalyst nucleation could be reduced. The metallic to semiconducting ratio is seen to again favor semiconducting tubes, as it is much lower than $1/3$, which was the ratio of chiralities which demonstrate metallic behavior. The films synthesized with $1100 \text{ } ^\circ\text{C}$ were also doped with AuCl_3 , since they showed promise in terms of conductivity. The R_{90} value gotten for this series of samples was approximately $77 \Omega/\square$ and the transmittance versus sheet resistance

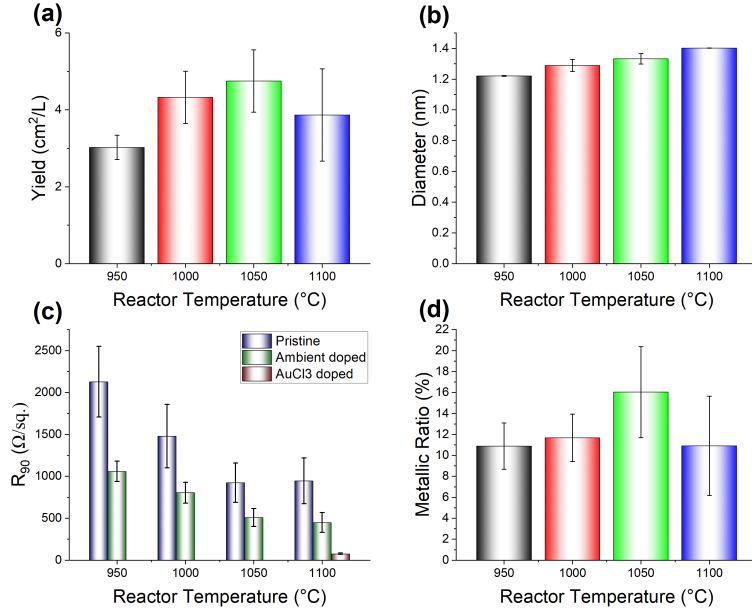


Figure 12: Bar graphs of (a) yield (b) mean tube diameter (c) sheet resistance at 90% transmittance (d) metallic ratio vs. reactor temperature.

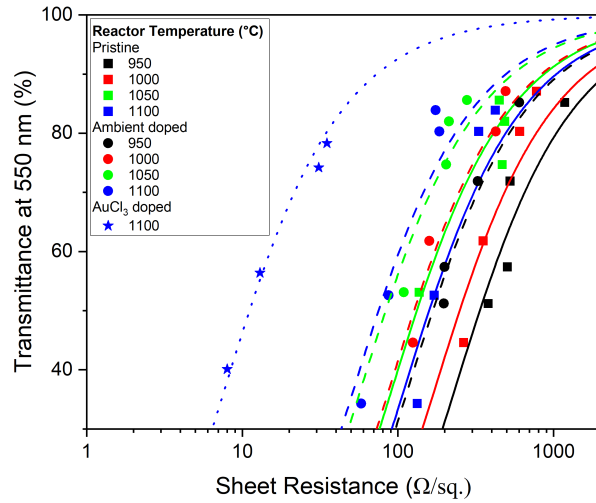


Figure 13: Transmittance vs. sheet resistance curves for pristine and doped values of different reactor temperatures.

curve for this can be seen in figure 13, where we see the doped curve is significantly improved compared with the others. This value is still significantly higher compared with ITO, but in the context of CNTs, it is considered low.

The Raman spectra for the different temperatures can be seen in figure 14a-c, where again the calculated diameters from the RBM peak coincide well with the

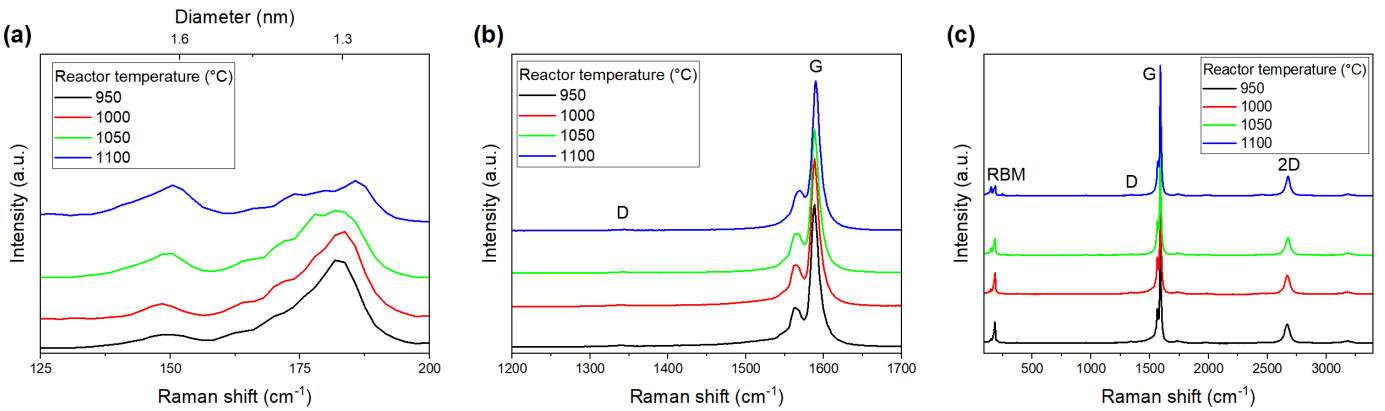


Figure 14: Raman spectra of CNT films synthesized with different reactor temperatures. (a) shows the RBM band (b) shows the D and G bands and (c) shows the whole spectra.

results gotten from the UV-Vis-NIR spectra. With lower temperatures, the distribution is seen to be mostly concentrated around 1.3 nm, and with higher temperatures we can see the distribution is wider, as was seen from the UV-Vis-NIR spectra. Much like before, the diameter distribution seems to have a lower bound at about 1.25 nm, the D-band is negligible and the G^- -band is pronounced.

4.4 Ferrocene content

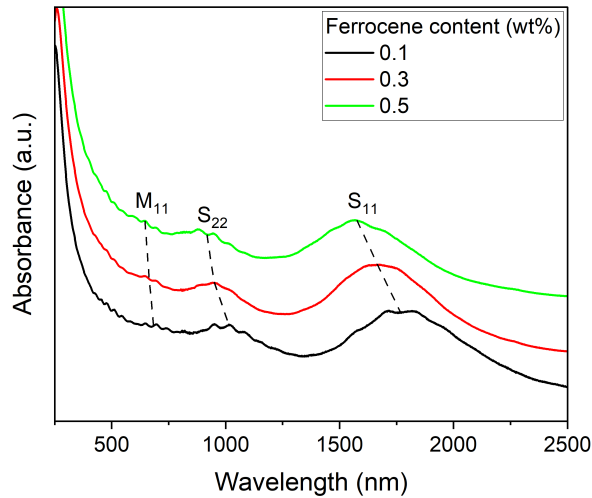


Figure 15: UV-Vis-NIR spectra of CNT films synthesized with different ferrocene contents.

The UV-Vis-NIR spectra for different ferrocene contents is seen in figure 15 where again we see significant ripples in the peaks and the peaks shifting to the left with

increasing ferrocene content. There also seems to be some visible peaks to the left of the M_{11} peak, which could correlate to higher band transitions such as the S_{33} peak, but they are not significantly visible in the spectra.

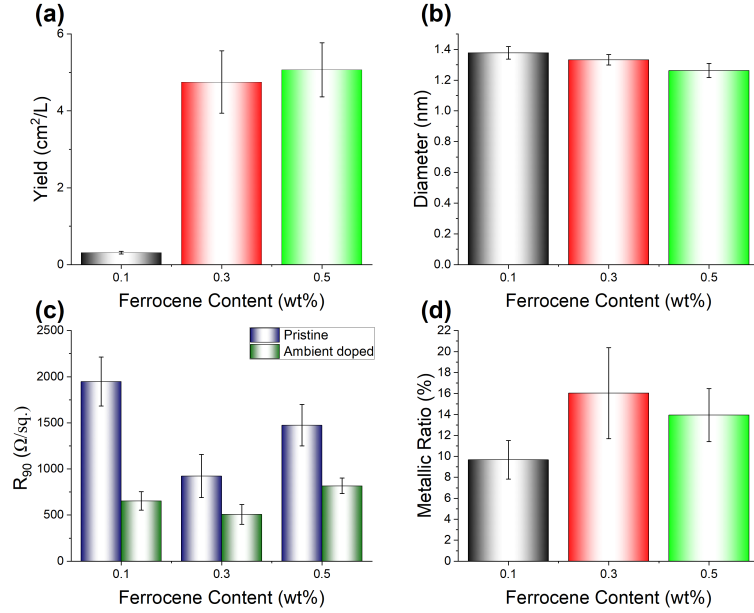


Figure 16: Bar graphs of (a) yield (b) mean tube diameter (c) sheet resistance at 90% transmittance (d) metallic ratio vs. ferrocene content.

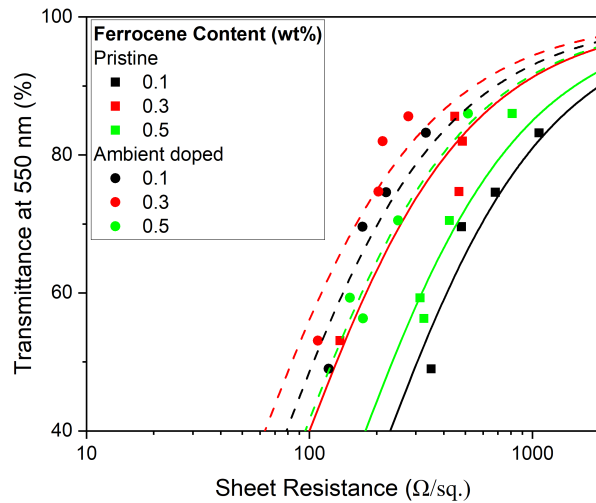


Figure 17: Transmittance vs. sheet resistance curves for pristine and doped values of different ferrocene contents.

The calculated quantities we can see in figure 16a-d, where we can see that the

yield of CNTs is significantly increased with increasing ferrocene content. This is expected, as a larger amount of ferrocene results in more active catalyst particles inside the reactor. The diameter is also observed to decrease, which could be due to the same phenomenon as with increasing the feeding rate, meaning a larger amount of aerosol inside the reactor resulting in a smaller average diameter. This is however unexpected, since usually increasing the ferrocene has been observed to result in larger catalyst particles and thus larger CNTs. As for the metallic ratios and R_{90} values, no improvement is seen from the baseline of 0.3 wt% and here the ambient doped values are also measured after a week. The same can be concluded from figure 17, where we see 0.3 remains the best in terms of conductivity when examining the fitted curves.

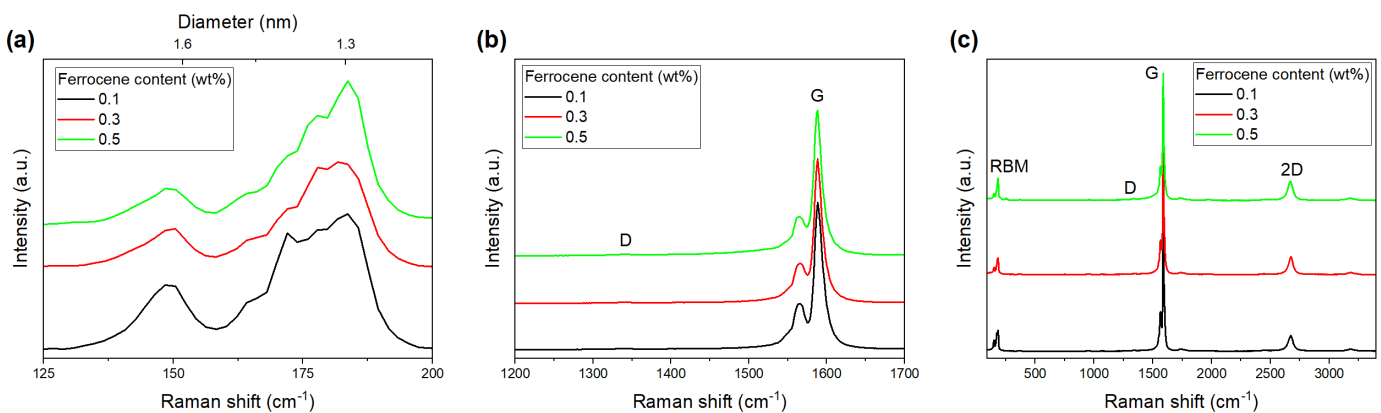


Figure 18: Raman spectra of CNT films synthesized with different ferrocene contents. (a) shows the RBM band (b) shows the D and G bands and c) shows the whole spectra.

The Raman spectra for the ferrocene contents used can be seen in 18, where similar conclusions can be drawn as before. The diameter distribution supports the results from the UV-Vis-NIR spectra and a lower bound is observed, the D-band is negligible and G^- -band is pronounced, indicating large amounts of CNTs.

4.5 Carrier gasses

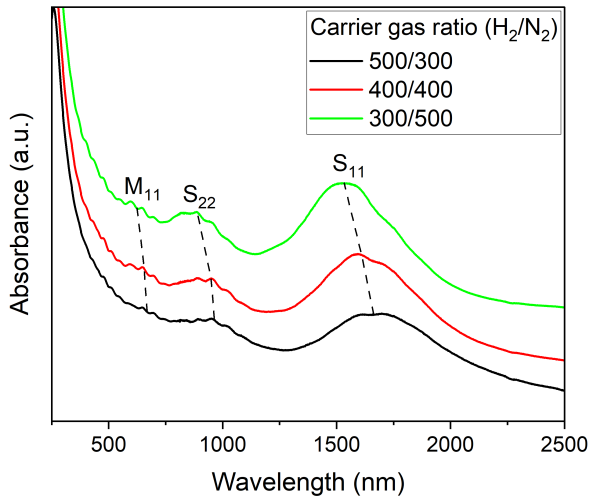


Figure 19: UV-Vis-NIR spectra of CNT films synthesized with different carrier gas ratios.

The UV-Vis-NIR spectra for different carrier gas ratios can be seen in figure 19, where inherent differences can be seen in the spectra, but they are minor as the difference between the ratios is not large. The peaks can be observed to shift left with decreasing hydrogen in the reactor atmosphere. The values presented in the legend correspond to flow rates used in SCCM, so the total flow was maintained at 800 SCCM and the ratio of hydrogen was altered from 37.5 % to 62.5 %.

The quantities calculated from the UV-Vis-NIR spectra and sheet resistance measurements can be seen in 20a-d, where we can see that the yield is considerably lower with higher amount of hydrogen. This could be due to the etching effect of hydrogen, which can remove carbons from the CNT during nucleation, which would decrease the yield [11]. This same effect could also be a reason why with higher hydrogen contents, we see a larger average diameter of CNTs. A hydrogen atmosphere could also reduce the decomposition temperature of sulfur sources, which would have an opposite effect on the diameter compared with the etching [19]. This could be why we see the diameter stagnating at about 1.3 nm with increasing the hydrogen, as the effects of etching and reduction in the decomposition temperature work against each other. Much like before, the values after doping are after a week of doping, and no improvement can be seen in R_{90} , which can also be seen from figure 21, or the metallic ratio.

The Raman spectra for different carrier gas ratios can be seen in figure 22a-c, where again the diameter distribution correlates with the values for the average diameter gotten from the UV-Vis-NIR spectra and a lower bound of about 1.25 nm is again observed. The D-band is negligible as before, indicating good quality of films and the G^- -band pronounced, as before, indicating high amounts of CNTs. The CNT

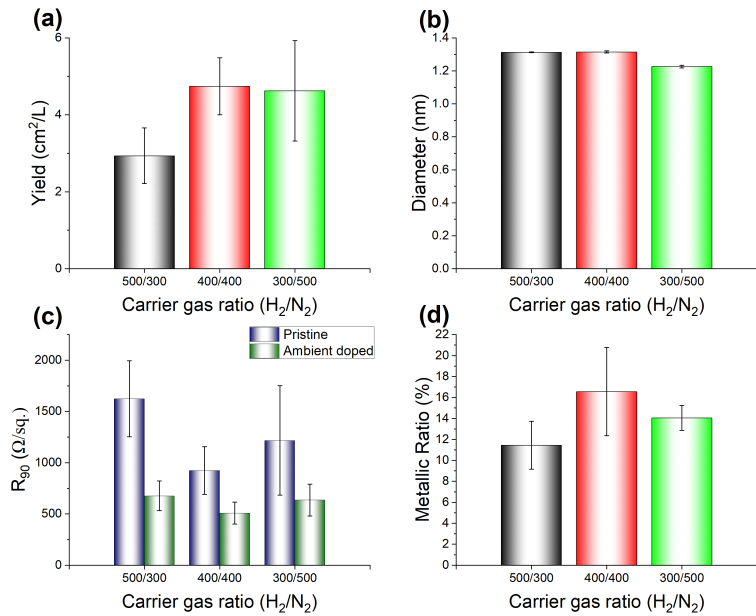


Figure 20: Bar graphs of (a) yield (b) mean tube diameter (c) sheet resistance at 90% transmittance (d) metallic ratio vs. carrier gas ratios.

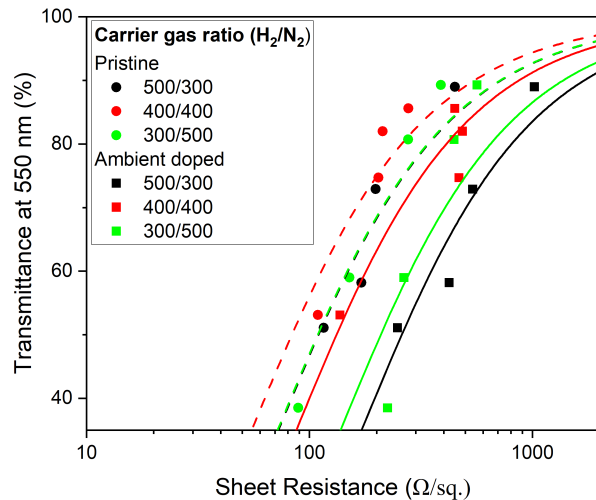


Figure 21: Transmittance vs. sheet resistance curves for pristine and doped values of different carrier gas ratios.

films synthesized with 300/500 of H_2/N_2 correspond to one of the smallest average diameters synthesized, along with the reactor temperature of 950 °C, and comparing these two we see a lot of similarities with a high intensity at 1.3 nm and a low intensity at 1.6 nm compared with the other conditions.

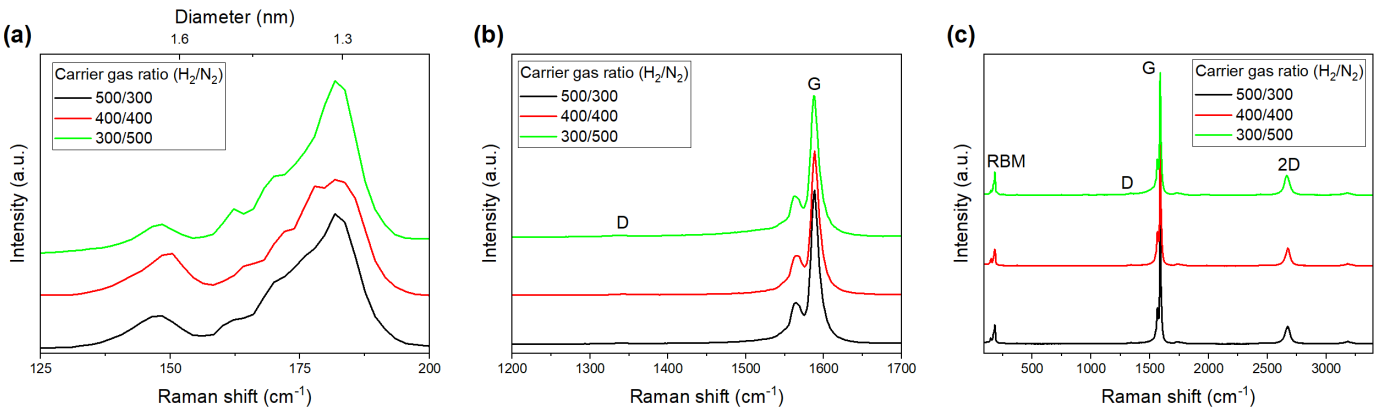


Figure 22: Raman spectra of CNT films synthesized with different carrier gas ratios. (a) shows the RBM band (b) shows the D and G bands and (c) shows the whole spectra.

5 Summary

The role of carbon disulfide as a growth promoter in the FCCVD synthesis of CNTs was thoroughly explored by varying multiple synthesis parameters, with a particular focus on the sulfur to iron molar ratio. The results indicate that CS_2 has a restrictive effect on the diameter of the synthesized CNTs, limiting them to approximately 1.3 nm, which differs significantly from the effects observed with the commonly used growth promoter, thiophene. This difference may enable possible future applications where specific CNT diameters are desirable.

To enhance the understanding of the effect of CS_2 , further studies should be carried out, including TEM analysis to determine diameter, bundle size and chirality distributions, as well as a comprehensive Raman analysis utilizing multiple lasers. Additionally, the feeding rate, which has shown a significant impact on CNT characteristics, should be further investigated.

The study attained a lowest sheet resistance of approximately $77 \Omega/\square$ at 90 % transmittance with a relatively low average diameter of 1.4 nm, which could be potentially optimized further for TCF applications. Despite years of research, the precise role of sulfur in CNT synthesis remains a matter of debate, thus highlighting the need for further studies and novel characterization methods to explore CNTs synthesized with different sulfur sources.

References

- [1] E. Ding, "Gas-phase synthesis of single-walled carbon nanotubes from liquid carbon source for transparent conducting film applications", PhD thesis, Aalto University, Department of Applied Physics, Espoo, Finland, 2019.
- [2] S. Rathinavel, K. Priyadarshini, and D. Panda, "A review on carbon nanotube: An overview of synthesis, properties, functionalization, characterization, and the application", Materials Science and Engineering: B, Volume 268, 2021, <https://doi.org/10.1016/j.mseb.2021.115095>.
- [3] Q. Zhang, N. Wei, P. Laiho, and E.I. Kauppinen, "Recent Developments in Single-Walled Carbon Nanotube Thin Films Fabricated by Dry Floating Catalyst Chemical Vapor Deposition", Topics in Current Chemistry, Volume 375, Article 90, 2017, <https://doi.org/10.1007/s41061-017-0178-8>.
- [4] M. Sehrawat, M. Rani, S. Sharma, S. Bharadwaj, B. G. Falzon, and B. Pratap Singh, "Floating catalyst chemical vapour deposition (FCCVD) for direct spinning of CNT aerogel: A review", Carbon, Volume 219, 2024, <https://doi.org/10.1016/j.carbon.2023.118747>.
- [5] A.R. Bogdanova, D.V. Krasnikov, and A.G. Nasibulin, "The role of sulfur in the CVD carbon nanotube synthesis", Carbon, Volume 210, 2023, <https://doi.org/10.1016/j.carbon.2023.118051>.
- [6] S. Iijima, "Helical microtubules of graphitic carbon", Nature, Volume 354, Pages 56–58, 1991, <https://doi.org/10.1038/354056a0>.
- [7] L. Boumia, M. Zidour, A. Benzair, and A. Tounsi, "A Timoshenko beam model for vibration analysis of chiral single-walled carbon nanotubes", Physica E: Low-dimensional Systems and Nanostructures, Volume 59, Pages 186–191, 2014 [10.1016/j.physe.2014.01.020](https://doi.org/10.1016/j.physe.2014.01.020).
- [8] J. Prášek, J. Drbohlavova, J. Pekarkova, J. Hubalek, O. Jašek, V. Adam, and R. Kizek, "Methods for carbon nanotubes synthesis - Review", Journal of Materials Chemistry, Volume 21, 2011, [10.1039/C1JM12254A](https://doi.org/10.1039/C1JM12254A).
- [9] A. Szabó, C. Perri, A. Csató, G. Giordano, D. Vuono, and J.B. Nagy, "Synthesis Methods of Carbon Nanotubes and Related Materials", Materials 2010, Volume 3, 2010, <https://doi.org/10.3390/ma3053092>.
- [10] K.A. Shah, and B.A. Tali, "Synthesis of carbon nanotubes by catalytic chemical vapour deposition: A review on carbon sources, catalysts and substrates", Materials Science in Semiconductor Processing, Volume 41, Pages 67-82, 2016, <https://doi.org/10.1016/j.mssp.2015.08.013>.
- [11] P.-X. Hou, F. Zhang, L. Zhang, C. Liu, and H.-M. Cheng, "Synthesis of Carbon Nanotubes by Floating Catalyst Chemical Vapor Deposition and

Their Applications", Advanced Functional Materials, Volume 21, 2022, <https://doi.org/10.1002/adfm.202108541>.

- [12] B. Orbána, and T. Höltzl, "The promoter role of sulfur in carbon nanotube growth", Dalton Trans., Volume 51, 2022, <https://doi.org/10.1039/D2DT00355D>.
- [13] A. Barreiro, S. Hampel, M.H. Rümmeli, C. Kramberger, A. Grüneis, K. Biedermann, A. Leonhardt, T. Gemming, B. Büchner, A. Bachtold, and T. Pichler, "Thermal Decomposition of Ferrocene as a Method for Production of Single-Walled Carbon Nanotubes without Additional Carbon Sources", The Journal of Physical Chemistry B, Volume 110, Pages 20973-20977, 2006, [10.1021/jp0636571](https://doi.org/10.1021/jp0636571).
- [14] T. Dzhapparov, and B.A. Ramazanovich, "Research of Thermal Stability of Water Mixtures of Aliphatic Alcohols", Journal of Materials Science and Engineering, Journal of Materials Science and Engineering A, Volume 2, Pages 786-790, 2018, [10.17265/2161-6213/2012.12.004](https://doi.org/10.17265/2161-6213/2012.12.004).
- [15] J. Park, R.S. Zhu, and M.C. Lin, "Thermal decomposition of ethanol. I. Ab Initio molecular orbital/Rice–Ramsperger–Kassel–Marcus prediction of rate constant and product branching ratios", The Journal of Chemical Physics, Volume 117, Pages 3224-3231, 2002, [10.1063/1.1490601](https://doi.org/10.1063/1.1490601).
- [16] M.D. Yadav, K. Dasgupta, A.W. Patwardhan, A. Kaushal, and J.B. Joshi, "Kinetic study of single-walled carbon nanotube synthesis by thermocatalytic decomposition of methane using floating catalyst chemical vapour deposition", Chemical Engineering Science, Volume 196, Pages 91-103, 2019, <https://doi.org/10.1016/j.ces.2018.10.050>.
- [17] F. Yu, M. Yang, F. Li, C. Su, B. Ma, Z. Yuan, J. Chen, and J. Ma, "The growth mechanism of single-walled carbon nanotubes with a controlled diameter", Physica E: Low-dimensional Systems and Nanostructures, Volume 44, Issue 10, 2012, <https://doi.org/10.1016/j.physe.2012.06.007>.
- [18] S.Y. Moon, I.J. Kang, S.M Kim, and W.S. Kim, "Influence of the Sulfur Content Catalyst on the Packing Density of Carbon Nanotube Forests", Nanomaterials, Volume 9, 2019, <https://doi.org/10.3390/nano9060889>.
- [19] M.D. Yadav, and K. Dasgupta, "Role of sulfur source on the structure of carbon nanotube cotton synthesized by floating catalyst chemical vapour deposition", Chemical Physics Letters, Volume 748, 2020, <https://doi.org/10.1016/j.cpl.2020.137391>.
- [20] M. Naftaly, S. Das, J.C. Gallop, K. Pan, F. Alkhalil, D. Kariyapperuma, S. Constant, C. Ramsdale, and L. Hao, "Sheet Resistance Measurements of Conductive Thin Films: A Comparison of Techniques", Electronics, Volume 10, 2021 [10.3390/electronics10080960](https://doi.org/10.3390/electronics10080960).

- [21] Y. Tian, H. Jiang, J. v. Pfaler, Z. Zhu, A.G. Nasibulin, T. Nikitin, B. Aitchison, L. Khriachtchev, D.P. Brown, and E.I. Kauppinen, "Analysis of the Size Distribution of Single-Walled Carbon Nanotubes Using Optical Absorption Spectroscopy", *The Journal of Physical Chemistry Letters*, Volume 1, Pages 1143-1148, 2010, [10.1021/jz100161p](https://doi.org/10.1021/jz100161p).
- [22] R. Rafiee, and A. Eskandariyun, "Comparative study on predicting Young's modulus of graphene sheets using nano-scale continuum mechanics approach", *Physica E: Low-dimensional Systems and Nanostructures*, Volume 90, Pages 42-48, 2017, <https://doi.org/10.1016/j.physe.2017.03.006>.
- [23] K. Wakabayashi, K.-i. Sasaki, T. Nakanishi, and T. Enoki, "Electronic states of graphene nanoribbons and analytical solutions", *Science and Technology of Advanced Materials*, Volume 11, 2010, <https://doi.org/10.1088/1468-6996/11/5/054504>.
- [24] Y. Miyata, K. Yanagi, Y. Maniwa, and H. Kataura, "Optical Evaluation of the Metal-to-Semiconductor Ratio of Single-Wall Carbon Nanotubes", *The Journal of Physical Chemistry C*, Volume 112, Pages 13187-13191, 2008, [10.1021/jp804006f](https://doi.org/10.1021/jp804006f).
- [25] I. Oshina, and J. Spigulis, "Beer-Lambert law for optical tissue diagnostics: current state of the art and the main limitations", *J Biomed Opt.*, Volume 26, 2021, [10.1117/1.JBO.26.10.100901](https://doi.org/10.1117/1.JBO.26.10.100901).
- [26] A. Jorio, and R. Saito, "Raman spectroscopy for carbon nanotube applications", *J. Appl. Phys.*, Volume 129, 2021, <https://doi.org/10.1063/5.0030809>.
- [27] E. M. Khabushev, "Fine-Tuning of Single-Walled Carbon Nanotube Properties for Transparent Conductive Applications", PhD thesis, Aalto University, Department of Chemistry and Materials Science, Espoo, Finland, 2022.
- [28] E.W. Chen, "Doping of Carbon Nanotubes", *Doped Nanomaterials and Nanodevices*, American Scientific Publishers, Volume 3, 2007.
- [29] K.-i. Sasaki, and Y. Tokura, "Theory of a carbon-nanotube polarization switch", *Physical Review Applied*, Volume 9, 2018, <https://doi.org/10.1103/PhysRevApplied.9.034018>.
- [30] B. Döring, S. Sandoval, P. Kankla, A. Fuertes, G. Tobias, and M. Campoy-Quiles, "Exploring different doping mechanisms in thermoelectric polymer/carbon nanotube composites", *Synthetic Metals*, Volume 225, Pages 70-75, 2017, <https://doi.org/10.1016/j.synthmet.2017.01.002>.
- [31] J.-W. Kang, S.-P. Lee, D.-G. Kim, S. Lee, G.-H. Lee, J. Kim, S.-Y. Park, J.H. Kim, and Y.-S. Jeong, "Reduction of Series Resistance in Organic Photovoltaic Using Low Sheet Resistance of ITO Electrode", *Electrochemical and Solid State Letters*, Volume 12, 2009, [10.1149/1.3055339](https://doi.org/10.1149/1.3055339).

- [32] A. Kaskela, A.G. Nasibulin, M.Y. Timmermans, B. Aitchison, A. Papadimitratos, Y. Tian, Z. Zhu, H. Jiang, D.P. Brown, A. Zakhidov, and E.I. Kauppinen, "Aerosol-Synthesized SWCNT Networks with Tunable Conductivity and Transparency by a Dry Transfer Technique", Nano Letters, Volume 10, Pages 4349-4355, 2010, [10.1021/nl101680s](https://doi.org/10.1021/nl101680s).

A Results tables

This appendix contains the results for each synthesis parameter study in individual tables. The values are rounded either to the nearest whole number or the nearest decimal, and particularly the diameter Range from Raman is only an approximate.

Table A1: Data on sulfur content and related quantities.

S/Fe	Metallicity (%)	Yield (cm ² /L)	R ₉₀ after a month of doping (Ω/□)	R ₉₀ AuCl ₃ doped (Ω/□)	Diameter from UV (nm)	Diameter range from Raman (nm)
0.2	11.6	0.6	926	94	1.96	1.5-2.6
0.3	12.2	1.0	338	90	1.43	1.2-1.8
0.6	16.6	1.9	342	154	1.32	1.2-1.8
0.9	16.7	3.2	331	114	1.32	1.2-1.8
1.5	16.4	2.7	1161	120	1.38	1.2-1.8
2.0	15.1	2.1	1047	125	1.40	1.2-1.8
3.0	15.3	2.2	932	112	1.40	1.2-1.8

Table A2: Data on reactor temperature and related quantities.

Reactor temperature (°C)	Metallicity (%)	Yield (cm ² /L)	R ₉₀ after a week of doping (Ω/□)	R ₉₀ AuCl ₃ doped (Ω/□)	Diameter from UV (nm)	Diameter range from Raman (nm)
950	10.9	3.0	1059	-	1.22	1.2-1.7
1000	11.7	4.3	804	-	1.29	1.2-1.7
1050	16.0	4.7	508	-	1.33	1.2-1.8
1100	10.9	3.9	449	77	1.40	1.2-1.8

Table A3: Data on ferrocene wt% and related quantities.

Ferrocene wt%	Metallicity (%)	Yield (cm ² /L)	R ₉₀ 1 week doping (Ω/□)	Diameter from UV (nm)	Diameter range from Raman (nm)
0.1	9.7	0.3	654	1.38	1.2-1.8
0.3	16.0	4.7	508	1.33	1.2-1.8
0.5	13.9	5.1	817	1.26	1.2-1.8

Table A4: Data on carrier gas ratio and related quantities.

Carrier gas ratio (H ₂ /N ₂)	Metallicity (%)	Yield (cm ² /L)	R ₉₀ 1 week doping (Ω/□)	Diameter from UV (nm)	Diameter range from Raman (nm)
500/300	11.4	2.9	677	1.31	1.2-1.8
400/400	16.6	4.7	508	1.32	1.2-1.8
300/500	14.0	4.6	636	1.23	1.2-1.8